(Received 4 October 2025, Accepted 1 December 2025, Scheduled 19 December 2025)

Research and Design of Non-Contact Electromagnetic Flowmeter

Jing Zeng[1], Haoxuan Xu[1], Hongjia Liu[2, 3, *], Jing Liu[2, 3], Yuanyuan Li[2, 3], Guoqiang Liu[2, 3], and Errun He[2, 3]

[1] *School of Information Engineering, Shenyang University of Chemical Technology, Liaoning 110142, China*
[2] *Institute of Electrical Engineering, Chinese Academy of Sciences, Beijing 100190, China*
[3] *University of Chinese Academy of Sciences, Beijing 100049, China*

ABSTRACT: Liquid metals possess significant application value in key sectors such as new energy, nuclear energy, and metallurgy due to their excellent fluidity, high electrical and thermal conductivity, and remarkable high-temperature stability. Accurate flow measurement during their application is crucial for ensuring system safety. However, conventional flow measurement techniques struggle to guarantee long-term stability under high-temperature conditions. To address this challenge, this paper proposes a non-contact alternating current excitation electromagnetic flowmeter. The design generates a stable alternating magnetic field via an excitation coil and employs externally mounted, differentially connected induction coils as the sensing element. This configuration enables non-contact measurement of liquid metal flow within metal pipes, fundamentally overcoming the reliability degradation issues associated with direct sensor contact with the measured medium. Experimental results demonstrate that the system has the potential to operate stably at a high temperature of 600°C and has achieved a high measurement accuracy of 3%.

1. INTRODUCTION

Liquid metal is a special functional material that exists in a liquid state at or near room temperature. It combines good fluidity, high electrical and thermal conductivity, and excellent high-temperature stability, thus demonstrating significant application value in key sectors such as the new energy, nuclear energy, and metallurgy industries. A team led by Donald Sadoway at the Massachusetts Institute of Technology (MIT) successfully developed a large-scale energy storage battery based on liquid metal [1]. This battery features low cost and high power capacity, offering a new technological path for grid-level energy storage [2]. In the nuclear energy industry, liquid metal is considered the "blood" of fourth-generation advanced nuclear reactors [3]. Both the lead-cooled fast reactor technology research led by the European Union and the Chinese lead-based reactor engineering design overseen by the Institute of Nuclear Energy Safety Technology under the Chinese Academy of Sciences select liquid lead-bismuth alloy as the primary circuit coolant. This leverages its excellent thermophysical properties to significantly enhance reactor safety and thermal efficiency. Furthermore, in the field of metallurgy, liquid metal is used as a high-performance quenching medium and an efficient extraction agent due to its exceptional thermal conductivity and high-temperature stability. In the various application processes mentioned above, real-time and accurate flow measurement of the liquid metal is crucial for ensuring the safety and stable operation of the systems. Monitoring flow abnormalities can help promptly identify potential safety hazards, thereby preventing accidents and ensuring long-term reliable system operation.

Currently, mainstream industrial flowmeters for liquid metal include orifice plate flowmeter [4], turbine flowmeter [5], ultrasonic flowmeter [6], and electromagnetic flowmeter. However, these flowmeters face numerous challenges when measuring high-temperature, highly corrosive liquid metals: The sensing elements of orifice plate flowmeter and turbine flowmeter, which need to be placed inside the pipeline, are highly susceptible to wear and erosion, leading to reduced accuracy and reliability [7]. Ultrasonic flowmeter, on the other hand, must overcome challenges related to probe durability at high temperatures [8]. Furthermore, the presence of bubbles or impurities in the liquid metal can cause signal scattering and attenuation, adversely affecting measurement accuracy. These factors collectively make their implementation in high-temperature environments both technically challenging and cost-prohibitive.

In contrast, due to the good electrical conductivity of liquid metal, electromagnetic flowmeter designed based on Faraday's law of electromagnetic induction is widely used for its measurement [9]. Traditional permanent magnet type electromagnetic flowmeter relies on permanent magnets to provide the steady magnetic field required for measurement [10]. However, permanent magnets are typically bulky and are susceptible to demagnetization at elevated temperatures, leading to a decay in magnetic field strength that compromises long-term measurement stability. Furthermore, this type of flowmeter utilizes a contact-based measurement approach with electrodes [11]. When measuring high-temperature, highly corrosive liquid metals, in addition to considering fluid conductivity and pipeline boundary conditions, it is crucial to address potential electrochemical corrosion at the electrode-fluid interface, along with spike noise interference resulting from fluid impact on the electrodes. These factors collectively reduce the mea-

* Corresponding author: Hongjia Liu (liuhongjia@mail.iee.ac.cn).

surement accuracy and operational stability of the flowmeter. Currently, there is a lack of fully mature solutions for measuring liquid metal flow in high-temperature environments.

To address the aforementioned issues, this paper presents a non-contact AC electromagnetic flowmeter using dual induction coils [12]. The sensor comprises an excitation coil and differential sensing coils [13]. The differential configuration is employed to effectively suppress common-mode interference. Both coils are wound on high-temperature-resistant ceramic formers using copper wires coated with an alumina (Al_2O_3) insulation layer, enabling stable operation at temperatures up to 600°C. In this design, a stable alternating magnetic field is generated by the excitation coil [14], while the differentially configured sensing coils, positioned externally on the pipeline, are used to detect alterations in the magnetic induction field caused by the flow of the liquid metal, thereby inducing an electromotive force. This structure can effectively avoid problems faced by traditional electromagnetic flowmeter, such as electrode corrosion, permanent magnet demagnetization, and fluid impact noise, consequently improving the flowmeter's measurement accuracy and stability. This flowmeter is not only simple in structure, high-temperature resistant, highly sensitive, and capable of long-term stable operation, but also small in size, easy to disassemble, and can be flexibly applied to different scenarios and pipes of various diameters.

2. THEORETICAL ANALYSIS

The electromagnetic flowmeter operates based on the principle of electromagnetic induction. Firstly, an alternating current is applied to the excitation coil to generate a corresponding alternating magnetic field in space, known as the primary magnetic field. When liquid metal moves within the magnetic field, according to Lenz's law, it induces a secondary magnetic field. This secondary magnetic field is then detected by two induction coils. By measuring the induced electromotive force (EMF) produced by each induction coil, the velocity of liquid metal is analyzed. The measurement principle is illustrated in Figure 1.

Liquid metal is typically modeled as media with constant electrical conductivity, isotropic magnetic permeability, and low flow velocity within the channel. The electromagnetic flow analysis can be decoupled into two independent processes: the actual physical process (Process I) and its reciprocal process (Process II). In Process I, the liquid metal flows at velocity $\mathbf{v}$ [15, 16], with coil A serving as the excitation source while coils B and C function individually as induction coils. In Process II, the liquid metal remains stationary, with coils B and C acting individually as excitation sources and coil A as the induction coil.

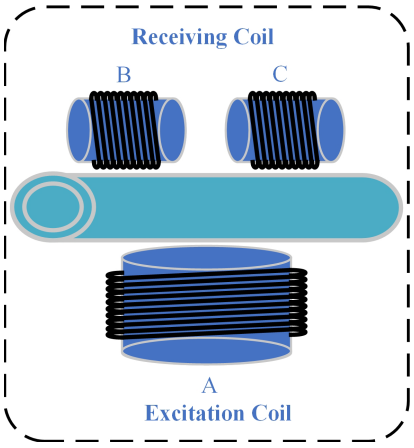

FIGURE 1. Schematic diagram of the non-contact electromagnetic flowmeter.

Based on these processes, the final expression simplifies to:

$$\xi_1^{\text{A->B}} - I_{1\text{B}}\xi_2^{\text{B->A}} = \int_V \mathbf{v}\cdot(\mathbf{J}_{2\text{B}}\times\mathbf{B}_{1\text{A}})\,\mathrm{d}V \tag{1}$$

$$\xi_1^{\text{A->C}} - I_{1\text{C}}\xi_2^{\text{C->A}} = \int_V \mathbf{v}\cdot(\mathbf{J}_{2\text{C}}\times\mathbf{B}_{1\text{A}})\,\mathrm{d}V \tag{2}$$

In the formulated equations, $I_{1\text{B}}$ and $I_{1\text{C}}$ represent the induced currents generated in Process I when Coil A serves as the excitation source, and Coils B and C act as receivers. Correspondingly, $\xi_1^{\text{A->B}}$ and $\xi_1^{\text{A->C}}$ denote the induced electromotive forces measured at Coils B and C during this process. In the reciprocal process (Process II), $\xi_2^{\text{B->A}}$ and $\xi_2^{\text{C->A}}$ are the induced EMFs measured at Coil A when Coils B and C individually function as excitation sources. The terms $\mathbf{J}_{2\text{B}}$ and $\mathbf{J}_{2\text{C}}$ (current density vectors) describe the distribution of induced current within the pipeline during Process II when Coils B and C excite the system, while $\mathbf{B}_{1\text{A}}$ signifies the magnetic flux density produced by Coil A as the excitation source in Process I. The variable v represents the flow velocity of liquid metal. Meanwhile, owing to the central symmetry of Coils B and C relative to Coil A, the relationship $I_{1\text{B}}\xi_2^{\text{B->A}} = I_{1\text{C}}\xi_2^{\text{C->A}}$ holds true, reflecting the geometric and electromagnetic symmetry in the system. By simultaneously solving the coupled Equations (1) and (2), the relationship between the induced EMF in induction Coil B or C and the flow velocity of liquid metal is derived as:

$$\xi_1^{\text{A->B}} - \xi_1^{\text{A->C}} = \int_V \mathbf{v}\cdot[(\mathbf{J}_{2\text{C}} - \mathbf{J}_{2\text{B}})\times\mathbf{B}_{1\text{A}}]\,\mathrm{d}V = \int_V \mathbf{v}\cdot\mathbf{F}\mathrm{d}V \tag{3}$$

wherein the measurement signal is proportional to the flow velocity $\mathbf{v}$, with its sensitivity defined by the weighting function $\mathbf{F}$. $\mathbf{F}$ is a weight function for the flow velocity $\mathbf{v}$, which is associated with coil parameter, excitation frequency flow velocity, and other factors.

3. SYSTEM OVERVIEW DESIGN

3.1. Detection System

The proposed detection system comprises an excitation coil, two induction coils, an excitation board, a detection board, and a host computer.

Both the excitation coil and induction coils are wound on high-temperature-resistant ceramic formers using aluminum oxide-coated copper wires, enabling stable operation in high-temperature environments up to 600°C. The coils are housed in

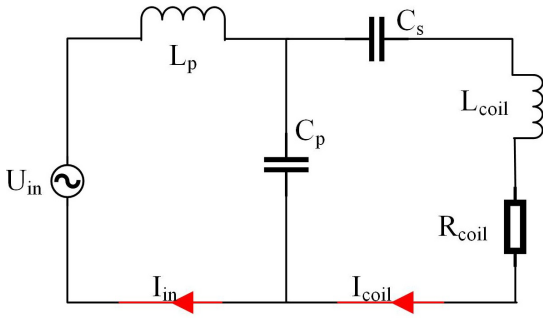

FIGURE 2. LCC resonant equivalent circuit diagram.

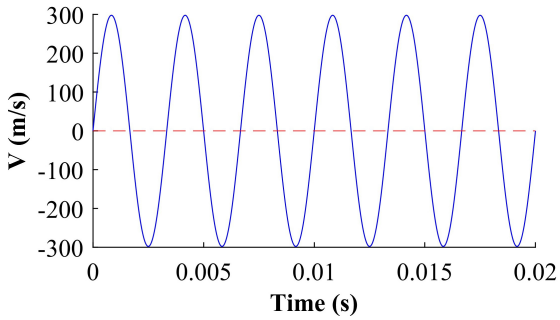

FIGURE 3. Excitation current waveform diagram.

stainless steel enclosures and fixed on both sides of the pipeline, providing effective shielding against external electromagnetic interference. This configuration results in a sensor that is structurally simple, compact, and easily detachable, facilitating its flexible application to pipelines of various diameters.

3.2. Design of Excitation Board

The excitation board comprises a DSP (Digital Signal Processor), an inverter circuit, an LCC resonant circuit, an Ethernet module, and four PWM driver circuits.

The DSP utilizes the TMS320F28023PTT as its control chip. It is primarily utilized to generate PWM signals for controlling the switching operations of NMOS transistors, and implement closed-loop PID control algorithm to dynamically regulate the output excitation current in real time.

Figure 2 illustrates the LCC resonant circuit. After determining the excitation signal frequency, the excitation coil serves as the resonant inductor. This coil, along with a compensating inductor of a specific value L_p, resonant compensation capacitors C_p, C_s and an equivalent AC voltage source, collectively form the LCC resonant circuit.

In Figure 2, the compensation device shall satisfy the following conditions:

$$j\omega L_p + \frac{1}{j\omega C_p} = 0 \tag{4}$$

$$j\omega L_{coil} + \frac{1}{j\omega C_s} + \frac{1}{j\omega C_p} = 0 \tag{5}$$

$$C_s = \frac{1}{\omega^2 (L_{coil} - L_p)} \tag{6}$$

To ensure that the calculated C_s is positive, the inductance L_{coil} of the external coil must always be greater than the inductance L_p of the compensation inductor. Assuming that the internal resistance of compensation inductor L_p is negligible, the coil current derived from Kirchhoff's Voltage Law is expressed as:

$$I_{coil} = \frac{U_{in}}{j\omega L_p} \tag{7}$$

the equivalent AC supply voltage U_{in} satisfies the following formula:

$$U_{in} = \frac{2\sqrt{2}}{\pi} U_d \sin\varphi \tag{8}$$

U_d is the DC supply voltage of the inverter, and φ is the phase shift angle of the inverter. When the compensating inductance L_p changes, the inverter can automatically adjust the phase shift angle φ to regulate the input voltage U_{in}, thereby ensuring that the output current I_{coil} remains constant.

3.2.1. Working Process

Firstly, the DSP generates a pair of complementary SPWM signals with dead time. These signals are amplified by the driving circuit to control the alternating switching of the four NMOS transistors in the full-bridge inverter. During the positive half-cycle, the upper bridge arm conducts to output a positive voltage, while the lower bridge arm conducts during the negative half-cycle to output a negative voltage, achieving bipolar modulation. The output is then processed through an LCC resonant circuit to maximize the retention of the fundamental sinusoidal signal at the target frequency, ensuring a pure AC output at a fixed frequency. A closed-loop PID control algorithm dynamically adjusts the output voltage's phase and amplitude in real time, stabilizing the excitation current with only minor fluctuations.

3.2.2. Excitation Current Measurement

To investigate the stability of the excitation current waveform (including key parameters such as amplitude and frequency) of an excitation coil in high-temperature environment, the following experimental procedure is designed: First, place the excitation coil into a high-temperature furnace. Heat the coil from room temperature at a constant power for 2 hours until its overall temperature uniformly reaches 600°C. Maintain a constant temperature of 600°C for 2 hours, followed by natural cooling. The excitation coil is driven by an external excitation board, while an oscilloscope coupled with a current probe is used to monitor and record the excitation current waveform in real-time at key temperature points. The results are shown in Table 1.

As shown in Table 1, the excitation current frequency remained stable at 300 Hz throughout the entire experimental process (from the start of heating until the end of natural cooling), with its amplitude maintained within a narrow range of 300 ± 2 mA. The corresponding waveform characteristics are depicted in Figure 3.

TABLE 1. Excitation current waveform parameters.

Condition	Temperature (°C)	Frequency (Hz)	Amplitude (mA)
Room Temperature	24	300	300 ± 0.5
Heating Process	300	300	300 ± 1.5
Maintained for 120 minutes	600	300	299 ± 1.0
Natural Cooling	30	300	300 ± 0.6

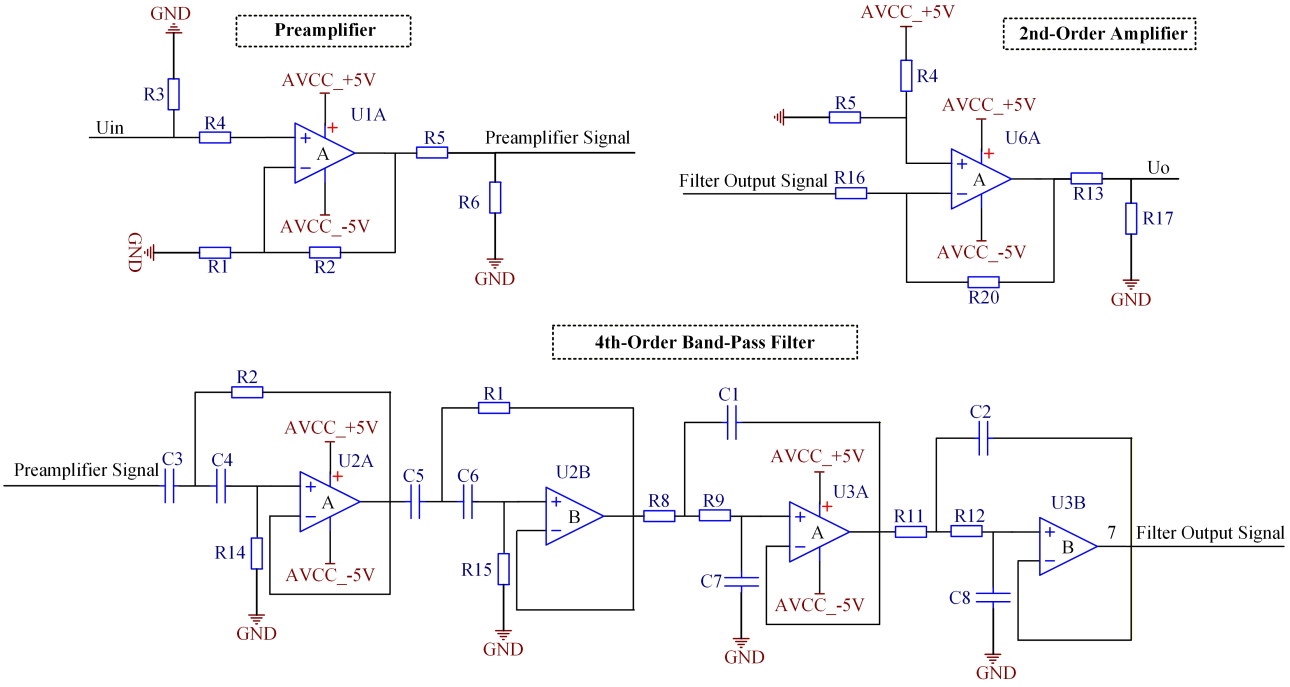

FIGURE 4. Signal conditioning circuit diagram.

3.3. Detection Board Design

The core processing unit of the detection board is the signal conditioning module. Since the induced electromotive force signal output by the induction coil is extremely weak and accompanied by complex noise interference, it cannot be directly converted by the ADC. The acquired signal must first undergo filtering and amplification processing before being converted into a digital signal by an analog to digital converter (ADC), and then sent to the STM32 for digital signal processing. The circuit schematic of the signal conditioning module is shown in Figure 4.

This circuit is composed of a preamplifier circuit, a filter circuit, and a 2nd-Order amplifier circuit. The primary function of the preamplifier circuit is to amplify the noise signals that are collected along with the input signal. It facilitates subsequent filtering processing. Therefore, the amplification factor A_1 should not be excessively high and is set to:

$$A_1 = \frac{R_{18} + R_{19}}{R_{18}} \tag{9}$$

For the filtering section, we adopted a filter based on the Butterworth type and the Sallen-Key topology. Simulate and design this circuit using Multisim software, with the filter gain set to 1, center frequency to 300 Hz, and bandwidth to 200 Hz. Due to its characteristics, the Butterworth filter exhibits a flat amplitude-frequency response within the passband. And it will become increasingly stable closer to the center frequency. Based on the simulated circuit parameters, soldering and testing were conducted on the hardware PCB board. The AFG port of the oscilloscope was connected to the input of the filter circuit, and sinusoidal signal with progressively increasing frequency was fed into the filter circuit. The amplitude-frequency characteristic was then analyzed, and the resulting response curve is shown in Figure 5.

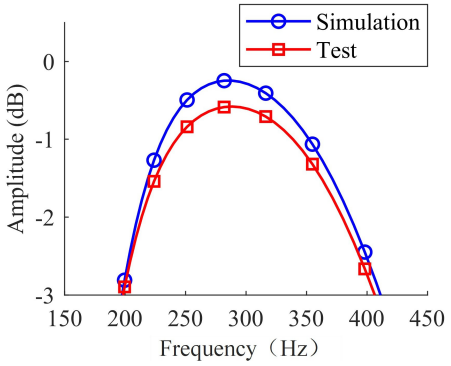

FIGURE 5. Amplitude-frequency response.

From the amplitude-frequency response curve in Figure 5, it is observed that the testing result is very close to the simulation result, meeting the design requirement.

The third section is a 2nd-Order amplifier circuit. After passing through the filter circuit, the input signal undergoes varying degrees of noise attenuation, but the effective signal remains relatively weak. Additionally, the amplitude of the input signal may be bipolar (positive and negative), while the sampling range of the ADC is 0–3.3 V. Therefore, the signal requires further amplification and the addition of a DC bias to level-shift it into the appropriate input range of the ADC. Its amplification factor A_2 and DC bias voltage U_{offset} are:

$$A_2 = \frac{R_{20}}{R_{16}} \tag{10}$$

$$U_{offset} = \frac{5R_5(R_{16} + R_{20})}{R_5 + R_4} \tag{11}$$

Since the signal transmitted by the signal conditioning module is analog signal, some special treatments of this module are required to preserve signal accuracy and minimize interference during transmission. To minimize temperature-induced errors, the signal conditioning module uses high-precision, low-drift components for all critical parts, specifically the operational amplifiers and precision resistors. Additionally, numerous thermal vias are added on the backside of the printed circuit board (PCB) beneath the analog components to further dissipate heat and mitigate temperature gradients. To enhance immunity to external electromagnetic interference (EMI), a metal shielding cover is installed over the entire signal conditioning module. Finally, a single-point common ground connection is employed to prevent ground noise from coupling between the digital and analog grounds, thereby significantly enhancing the module's operational stability.

4. RESULTS

4.1. Experiments and Methods

The experimental system is shown in Figure 6. It comprises a sensor, a detection board, an excitation board, an upper computer, and an electromagnetic pump. Prior to the experiment, the designed excitation board and detection board are correctly connected to the sensor. The connected sensors are then mounted at the upper and lower ends of a 34-mm-diameter pipeline, and the system is prepared for testing. The experiment is at room temperature ($25 \pm 2°$C). And the medium inside the pipeline is Galinstan alloy, and its electrical conductivity at the experimental temperature is approximately $3.46 \times 106\,\mathrm{S{\cdot}m^{-1}}$.

First, functional tests are conducted on the hardware, firmware, and host computer software to verify the correct and stable operation of the system. After the system functional tests are completed, the excitation current frequency is set to 300 Hz with an amplitude of 300 mA, and the electromagnetic pump is started to begin the experiment. During the experiment, the flow velocity of the liquid metal can be controlled by adjusting the operating current of the electromagnetic pump.

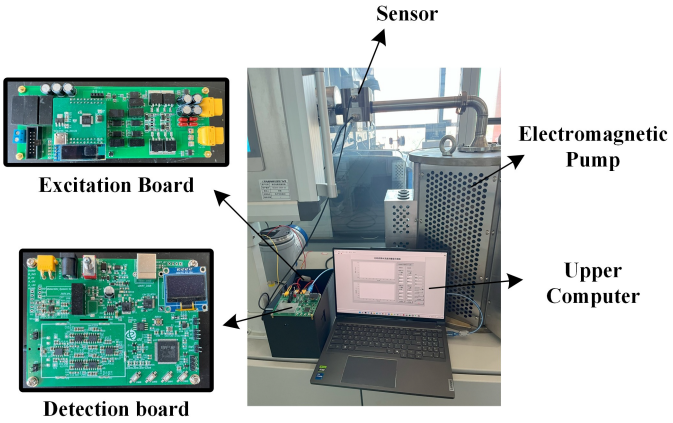

FIGURE 6. Schematic diagram of the electromagnetic flowmeter detection system.

4.2. System Testing

Continuous flow velocity measurements within the same pipeline segment were conducted at a set point of 1 m/s. Measurements were logged every 30 minutes, and the stability of the system's measurements was evaluated by analysing the variation between consecutive data points over time when the flow rate remains constant, the flow rate values detected by the system during long-term operation are highly consistent, with an error range within 3%. Additionally, the system response time is 1.52 s.

To evaluate the measurement accuracy, the flow velocity of the liquid metal in the pipeline was regulated by controlling the electromagnetic pump. The system sampled the flow velocity at 0.5 s intervals and compared it with a preset reference value to validate the measurement precision. The comparison results between the measured data and reference flow velocity are detailed in Figure 7.

As shown in Table 2, the dynamic response characteristics include: average flow velocity, relative standard deviation (RSD), and root mean square error (RMSE). Analysis indicates that as the flow velocity increases, the accuracy of the measurement system continuously improves. Under low flow velocity conditions (0.5 m/s), the measurement variability is relatively high, with RSD and RMSE reaching 2.86% and 2.88%,

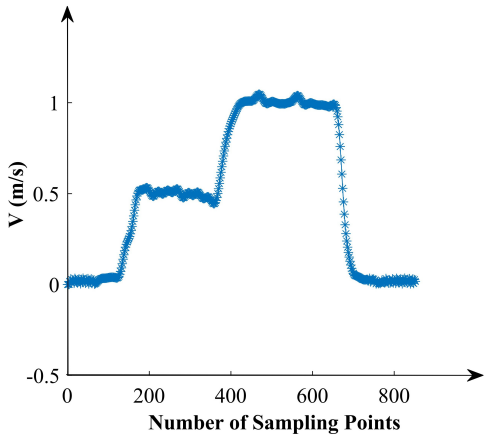

FIGURE 7. The measurement results of the flow velocity.

TABLE 2. Analysis of the dynamic characteristics.

Reference Velocity (m/s)	Mean Velocity (m/s)	RSD	RMSE
0.5	0.5061	2.86%	2.88%
1.0	1.0042	1.62%	1.68%

respectively. When the flow velocity increases to 1.0 m/s, the system performance shows significant improvement: RSD decreases markedly to 1.62%, and RMSE is reduced to 1.68%. This demonstrates a synchronous enhancement in both measurement precision and accuracy. In conclusion, the system achieves good measurement precision, with the overall error across all operational conditions controlled within 3%, meeting the design expectations.

5. CONCLUSION

This study presents the design of a non-contact electromagnetic flowmeter intended for operation in high-temperature and highly corrosive environments. The design generates a stable alternating magnetic field via an excitation coil and employs externally mounted, differentially connected induction coils as the sensing element. This configuration enables non-contact measurement of liquid metal flow within metal pipes, fundamentally overcoming the reliability degradation issues associated with direct sensor contact with the measured medium. The experimental results indicate that the key parameters of the flowmeter, such as the frequency and amplitude of the excitation current, remained stable within the design tolerance range during high-temperature testing at 600°C, and the total measurement error did not exceed 3%. This demonstrates that the design exhibits satisfactory operational stability and measurement accuracy.

Nevertheless, the experimental investigation was predominantly centered on the short-term tolerance of core components (such as the excitation coil), thus lacking a comprehensive evaluation of the system's long-term stability and integrated performance under continuous high-temperature exposure. Additionally, this study was limited by the available experimental equipment, which only allowed for testing at two flow velocities: 1 m/s and 0.5 m/s. Consequently, the limited amount of data collected may not fully capture the versatility, robustness, and accuracy of the proposed solution in actual, complex operating environments.

Addressing these limitations, future research efforts will be directed towards designing and conducting prolonged, system-level high-temperature endurance tests. Furthermore, studies involving an expanded sample size will be undertaken to facilitate a more robust statistical analysis, thereby enabling a comprehensive assessment of long-term stability and accuracy. These steps are crucial for advancing the technology to maturity and facilitating its broader application.

ACKNOWLEDGEMENT

This work was supported by the National Natural Science Foundation of China under Grant No. 52377018, and the Science and Technology Research Foundation of Institute of Electrical Engineering of Chinese Academy of Sciences under Grant No. IEERF250202.

REFERENCES

[1] Wang, K., K. Jiang, B. Chung, T. Ouchi, P. J. Burke, D. A. Boysen, D. J. Bradwell, H. Kim, U. Muecke, and D. R. Sadoway, "Lithium-antimony-lead liquid metal battery for grid-level storage," *Nature*, Vol. 514, No. 7522, 348–350, 2014.

[2] Zhu, Z., T. Jiang, M. Ali, Y. Meng, Y. Jin, Y. Cui, and W. Chen, "Rechargeable batteries for grid scale energy storage," *Chemical Reviews*, Vol. 122, No. 22, 16 610–16 751, 2022.

[3] Agbevanu, K. T., S. K. Debrah, E. M. Arthur, and E. Shitsi, "Liquid metal cooled fast reactor thermal hydraulic research development: A review," *Heliyon*, Vol. 9, No. 6, e16580, 2023.

[4] Martelli, D., A. Del Nevo, P. Agostini, M. Tarantino, *et al.*, "Development of lead-cooled fast reactor technologies at ENEA brasimone research center," *Arabian Journal for Science and Engineering*, Vol. 50, No. 5, 3293–3301, 2025.

[5] Wu, Y., Y. Song, Q. Huang, Z. Zhao, and L. Hu, "Development strategy and conceptual design of China lead-based research reactor," *Annals of Nuclear Energy*, Vol. 87, 511–516, 2016.

[6] Gao, Y., M. Chen, Z. Wu, L. Yao, Z. Tong, S. Zhang, Y. A. Gu, and L. Lou, "A miniaturized transit-time ultrasonic flowmeter based on ScAlN piezoelectric micromachined ultrasonic transducers for small-diameter applications," *Microsystems & Nanoengineering*, Vol. 9, No. 1, 49, 2023.

[7] Tang, Z., N. Jin, W. Ren, T. Pan, and L. Bai, "Measurement of liquid-liquid flows using turbine flowmeter and conductance sensor with multiheight electrodes in vertical pipes," *IEEE Transactions on Instrumentation and Measurement*, Vol. 72, 1–13, 2023.

[8] Sahu, S., K. Bhope, A. Prajapati, M. Mehta, H. Tailor, R. Bhattacharyay, and S. S. Khirwadkar, "Sonic velocity measurement in molten Pb-Li(16) at high temperature for ultrasonic flowmeter applications," *Flow Measurement and Instrumentation*, Vol. 88, 102271, 2022.

[9] Mohindru, P., "Recent advancements in volumetric flow meter for industrial application," *Heat and Mass Transfer*, Vol. 59, No. 11, 2149–2166, 2023.

[10] Wang, Z., S. Wang, X. Wang, and X. Luo, "Permanent magnet-based superficial flow velometer with ultralow output drift," *IEEE Transactions on Instrumentation and Measurement*, Vol. 72, 1–12, 2023.

[11] Gao, S. and H. Ma, "A study on structure improvement scheme of electromagnetic flow sensor for slurry flow measurement," *Measurement and Control*, Vol. 55, No. 5-6, 519–534, 2022.

[12] Mitchell, B., Y. Zhou, M. P. Hayes, B. Heffernan, I. Platt, J. Bailey, A. Hunze, K. Gao, N. Long, and I. Woodhead, "Non-invasive groundwater velocity measurements using a novel electromagnetic flowmeter," *IEEE Transactions on Instrumentation and Measurement*, Vol. 71, 1–15, 2022.

[13] Xiao, Q., J. Feng, Z. Xu, and H. Zhang, "Receiver signal analysis on geometry and excitation parameters of remote field eddy current probe," *IEEE Transactions on Industrial Electronics*, Vol. 69, No. 3, 3088–3098, 2022.

[14] Ge, L., S. Zhou, X. Xiao, W. Zeng, and K. Huang, "Research on optimization technology of excitation coil in downhole an-

nular flow electromagnetic measurement system," *Measurement Science and Technology*, Vol. 35, No. 3, 035121, 2024.

[15] Zhang, L.-F., C.-B. Wu, J.-Z. Liu, W.-Q. Qin, and Z.-H. Tang, "Analysis of spatial coupling behavior in gas-liquid two-phase flow within vertical upward pipelines," *Physics of Fluids*, Vol. 37, No. 6, 063344, 2025.

[16] Cheng, B., M. Tong, Q. Yan, B. Jin, N. Liu, and J. Lu, "Portable intelligent electromagnetic flowmeter controlled by magnetic induction intensity," *Electronics*, Vol. 13, No. 3, 556, 2024.